Spectral coarse graining and rescaling for preserving structural and dynamical properties in graphs

M. Schmidt, F. Caccioli, and T. Aste
Department of Computer Science, University College London, United Kingdom

(Received 20 December 2024; accepted 11 August 2025; published 2 September 2025)

We introduce a graph renormalization procedure based on the coarse-grained Laplacian, which generates reduced-complexity representations across scales. This method retains both dynamics and large-scale topological structures, while reducing redundant information, facilitating the analysis of large graphs by decreasing the number of vertices. Applied to graphs derived from electroencephalogram recordings of human brain activity, our approach reveals collective behavior emerging from neuronal interactions, such as coordinated neuronal activity. Additionally, it shows dynamic reorganization of brain activity across scales, with more generalized patterns during rest and more specialized and scale-invariant activity in the occipital lobe during attention.

DOI: 10.1103/k4bx-w273

I. INTRODUCTION

Graphs capture the intricate relationships and dynamics between the units that make up a complex system, such as the brain. As such, they are powerful tools for analyzing and modeling these systems. However, different properties of complex systems emerge at different scales, making it useful to scale out of the graph structure through coarse graining.

Coarse graining scales out by aggregating clusters of vertices and edges, leading to a simplified structural representation that preserves key features of the original system. To ensure that these simplified representations remain true to the underlying dynamics of the system, we propose a coarse-graining and rescaling procedure for graphs, inspired by the Renormalization Group [1], which does not rely on geometric closeness. This graph renormalization can reveal patterns and behaviors—such as collective neural activity—that may only become apparent at certain scales. As we look at the graph Laplacian, our method follows the direction pointed out by Ref. [2]'s Laplacian renormalization group scheme (LRG) and the spectral methods of Refs. [3–5]. However, instead of relying on the normalized heat kernel [6], we rely on the graph Laplacian itself to determine effective vertices representing groups of vertices that share much information and effective interactions between them. This results in a representation with both a coarse-grained structure and scale-adjusted weights, preserving large-scale topological structures while better preserving the underlying dynamics. Since dynamical processes provide a notion of distance, this is consistent with the ideas of Ref. [1], as we do not change the "distance" between the vertices or the "size" of the system in a physical sense.

The Renormalization Group (RG) [1,7] allows us to study how collective behavior in complex systems arises at different scales. It is fundamental for understanding critical phenomena, phase transitions, universality, and scale dependence. Intuitively, the RG is a tool to move from the microscopic to the macroscopic by coarse graining and rescaling the system, resulting in a simplified representation of the system [1,7–9]. For ferromagnets, coarse graining relies on geometric distance in a metric space, as the strength of interactions is highest between the closest spins. However, in many complex systems, closeness in a metric sense may not be the primary factor driving interactions. This is, for example, the case of the brain, which is composed of nonlinear interacting neurons that form synaptic connections across distances. We consider it as a use case and construct a graph representation based on the mutual information between electrode signals from electroencephalogram (EEG) recordings, capturing the functional dependencies between different brain regions and representing the interaction structure governing brain dynamics.

Applying the RG to such heterogeneous graphs poses significant challenges, as they do not have the homogeneous topology upon which the RG relies. Important efforts, besides Refs. [2,10–13]'s LRG to extend the RG to graphs through diffusion using the normalized heat kernel [6,14], were made by Ref. [15], which hypothesized the existence of an embedding space responsible for the graph structure. This underlying space allows for identifying "supernodes," providing a coarse-grained graph description, akin to block spins in the real-space RG [7]. Also, the approach in Ref. [16] embeds graphs into underlying metric geometrical spaces.

However, graphs are topological structures, and thus a topological notion of the RG is needed [17], which the graph Laplacian can provide.

II. CHARACTERISTIC SCALES AND GAPS IN THE LAPLACIAN SPECTRUM

We consider an undirected graph $G = (V, E)$, where V is the vertex set and E is the edge set. Its graph Laplacian is defined as $\mathbf{L} = \mathbf{D} - \mathbf{A} \in \mathbb{R}^{|V|\times|V|}$, where $\mathbf{A}$ is the adjacency matrix and $\mathbf{D}$ is the degree matrix. From the perspectives

Published by the American Physical Society under the terms of the Creative Commons Attribution 4.0 International license. Further distribution of this work must maintain attribution to the author(s) and the published article's title, journal citation, and DOI.

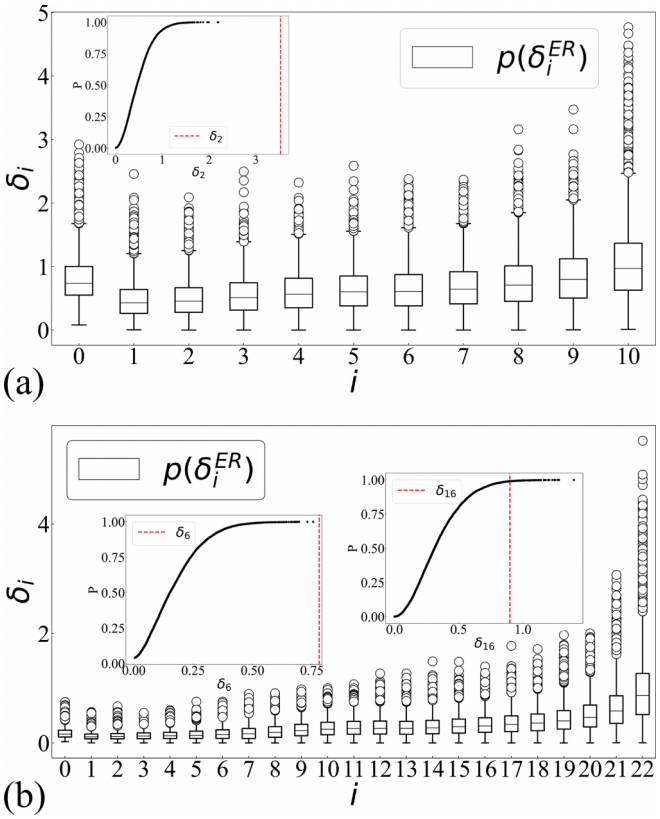


FIG. 1. Gaps $\delta_k = |\lambda_{k+1} - \lambda_k|$ in the Laplacian spectrum of graph (I) and graph (II) are examined by comparing each gap to the corresponding distribution $p(\delta_k^{\mathrm{ER}})$ of an ensemble of Erdős-Rényi graphs. (a) The gap distributions of an ensemble of 10^4 Erdős-Rényi graphs with the same expected average degree and number of vertices as graph (I). The cumulative distribution function (CDF) of gap 2 from the Erdős-Rényi ensemble is compared to the corresponding gap of graph (I), indicating a candidate gap in the Laplacian spectrum. (b) The gap distributions of an ensemble of 10^4 Erdős-Rényi graphs with the same expected average degree and number of vertices as graph (II). The CDFs of gaps 6 and 16 from the Erdős-Rényi ensemble are compared to the corresponding gaps of graph (II), indicating candidate gaps in the Laplacian spectrum.

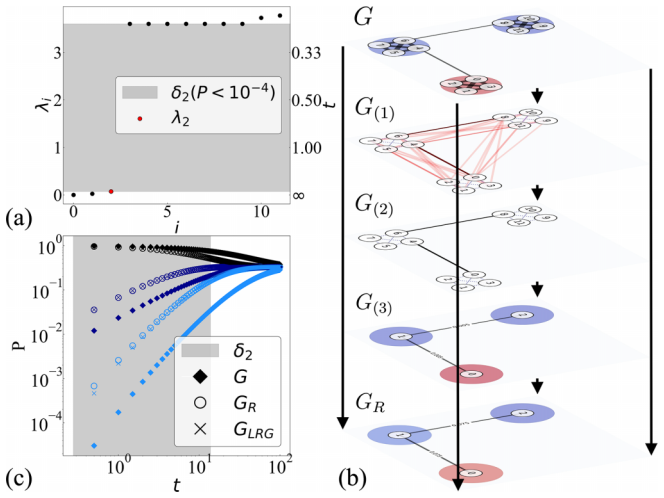


FIG. 2. Gap, dynamics, and renormalization of graph (I). (a) The first candidate (p value < 0.01) gap δ_2 of the graph Laplacian of G indicates the scale λ_2 to zoom out to using Eq. (2). (b) This results in $G_{(1)}$, which represents vertex similarities from a zoomed-out perspective, where positive weights (red line) indicate dissimilar vertices not connected in the original graph, while positive weights (black line) indicate dissimilar vertices connected in the original graph. Negative weights (blue dotted line) indicate similar vertices connected in the original graph. Thus, they can be contracted into effective vertices. This is achieved by assigning $G_{(1)}$'s weights to G using Eq. (5), resulting in $G_{(2)}$, and then contracting vertices connected by a blue edge, resulting in $G_{(3)}$. The new effective weights reflect that fast modes have been removed by Eq. (2). Thus, $G_{(1)}$ indicates how to derive a coarse-grained representation of the structure and dynamics of G. However, zooming out reduces resolution. To restore the original sharpness, we adjust the focus by rescaling the weights using Eq. (6), resulting in the renormalized graph G_R. The rescaling approximately preserves the original dynamics. (c) We show this by comparing the states $\mathbf{p}(t)$ of the clusters (original graph G) and effective vertices (renormalized graphs G_R or G_{LRG}). These states are determined by Eq. (1), with $\mathbf{p}(0)$ representing the cluster or effective vertex highlighted in red. The graph G_R is obtained using our procedure with $\lambda_2 = 0.07$, while G_{LRG} is obtained using Refs. [2]'s Wilsonian LRG with $\lambda^* = 1/0.79$ (identified by specific-heat peak [2]). Each color represents a different effective vertex or cluster. Closer alignment between points of the same color of G_R or G_{LRG} with G indicates better preservation of dynamics. The goodness depends on λ_{k+1} and δ_k [see Eq. (3)].

of matrix perturbation theory and spectral clustering, the characteristic scale to zoom to is determined by identifying the smallest k such that the corresponding gap $\delta_k = |\lambda_{k+1} - \lambda_k|$ between the eigenvalues $\lambda_0 \leqslant \lambda_1 \leqslant \lambda_2 \leqslant \ldots$ of the graph Laplacian $\mathbf{L}$ is anomalously large [3,18–20]. In practice, one possibility is to flag a single gap as potentially anomalous if its p value with respect to a null model is below $\alpha = 0.01$. This allows us to define an exploratory heuristic to discard most gaps attributable to noise and to suggest candidate gaps.

An ensemble of 10^4 connected Erdős-Rényi (ER) graphs $G_{\mathrm{ER}}(n, p)$, with the same number of vertices and same expected average degree as the original graph G, serves as the null model since they are structureless beyond randomness [21,22]. To illustrate the procedure, we consider graph (I), which consists of three 4-cliques with weights 0.9 connected by edges of weight 0.1 [see Fig. 2(b)], and graph (II), a Barabási-Albert graph with 24 vertices whose thick edges have weight 0.9 and thin edges 0.1 [see Fig. 3(b)]. For each graph we generate 10^4 Erdős-Rényi graphs $G_{\mathrm{ER}}^{(j)}(n, p)$, $j = 1, \ldots, 10^4$, with $n = |V|$ and $p = \frac{\langle k \rangle}{n-1}$, where $\langle k \rangle$ is the average degree of G. For every realization $G_{\mathrm{ER}}^{(j)}(n, p)$ we compute its spectrum $\{\lambda_i^{ER,(j)}\}_{i=0}^{n-1}$ and the corresponding eigenvalue gaps $\{\delta_i^{\mathrm{ER},(j)}\}_{i=0}^{n-2}$. Thus, for each gap index i we obtain 10^4 instances of gaps $(\delta_i^{\mathrm{ER},(j)})_{j=1}^{10^4}$, resulting in a gap distribution $p(\delta_i^{\mathrm{ER}})$ for each gap index i (see Fig. 1). Next, we compute the spectrum $\{\lambda_i\}_{i=0}^{n-1}$ and the gaps $\{\delta_i\}_{i=0}^{n-2}$ of the graph G. Each observed gap δ_i is compared with the corresponding gap distribution $p(\delta_i^{\mathrm{ER}})$ of the Erdős-Rényi ensemble, and the one-tailed empirical p value is computed. The gap-specific p value represents the probability of observing a gap as large as, or larger than, the observed one if the gap-specific null

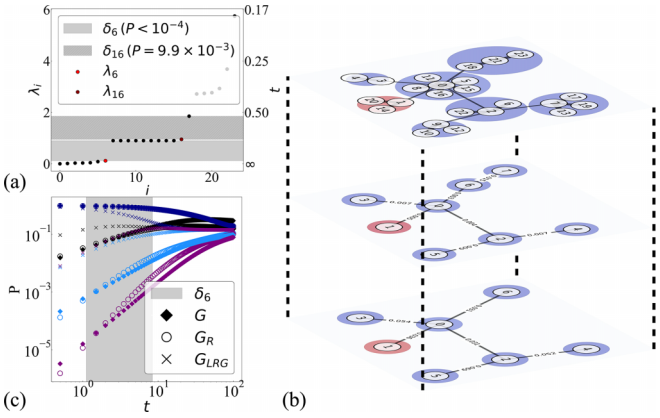


FIG. 3. Gap, dynamics, and renormalization of graph (II). (a), (b) Renormalized graphs are obtained for the first two candidate (p-value <0.01) gaps. (c) The states $\mathbf{p}(t)$ of the clusters (original graph G) and effective vertices (renormalized graphs G_R or G_{LRG}) are determined by Eq. (1), with $\mathbf{p}(0)$ representing the cluster or effective vertex highlighted in red. The graph G_R is obtained using our renormalization procedure with $\lambda_6 = 0.12$, while G_{LRG} is obtained using Ref. [2]'s Wilsonian LRG with $\lambda^* = 1/2.79$ (identified by specific-heat peak [2]). Each color represents a different effective vertex or cluster. We consider the renormalized graph associated with the first candidate gap and omit the clusters and the corresponding effective vertices 3, 4, and 6 for clarity. Closer alignment between points of the same color of G_R or G_{LRG} with G indicates that the dynamics are better preserved.

hypothesis were true. Here, the null hypothesis is that the observed gap comes from the same distribution as the gaps from the Erdős-Rényi graphs. A gap with gap-specific p value smaller than the gap-specific threshold α is flagged as a candidate. For graph (I), we find one candidate gap in the Laplacian spectrum, δ_2 with p value $<10^{-4}$. For graph (II), we find two candidate gaps in the Laplacian spectrum, δ_6 with p value $<10^{-4}$, and δ_{16} with p value $= 9.9 \times 10^{-3}$.

III. RENORMALIZATION

To obtain a representation of the system for the characteristic scale, interactions must be adjusted to preserve both dynamics and important structural properties at larger scales. Thus, we introduce a renormalization procedure using a rescaled coarse-grained Laplacian. Its ability to determine effective vertices and the effective weights between them can be understood by projecting the graph Laplacian into the subspace spanned by the eigenvectors associated with the k-smallest eigenvalues.

We project $\mathbf{L}$, which is represented in $\mathcal{E} = \mathrm{span}(\{\mathbf{e}_l\}_{l=0}^{|V|-1})$, where $\mathbf{e}_l \in \mathbb{R}^{|V|}$ is a standard basis vector, into space $\mathcal{S} = \mathrm{span}(\{\mathbf{u}_\alpha\}_{\alpha=0}^{|V|-1})$, where $\mathbf{u}_\alpha$ are the orthonormal eigenvectors of $\mathbf{L}$, via the spectral decomposition of the graph Laplacian $\mathbf{L} = \sum_\alpha \lambda_\alpha \mathbf{u}_\alpha \mathbf{u}_\alpha^\top$. By considering the eigenvectors as modes that indicate graph partitions, we can see that the Laplacian in $\mathcal{S}$ provides insights into the graph structure at different scales: For a connected graph, the eigenvector $\mathbf{u}_0$ represents a mode of the graph's overall connectivity structure. The eigenvector $\mathbf{u}_1$, also known as the Fiedler vector, represents a mode partitioning the graph into two. Higher-order eigenvectors $\mathbf{u}_{\alpha>1}$ correspond to modes representing finer partitions of the graph, associated with sign and magnitude patterns in the mode $\mathbf{u}_{\alpha>1}$ [3]. So, smaller eigenvalues correspond to smoother modes and coarser partitions. This can be explicitly seen as follows: Given a dynamical process on the graph, its state at dimensionless time t can be expressed by a vector $\mathbf{p}(t)$, whose interpretation depends on the specific process. This could be, for example, the amount of information associated with each vertex at time t. The state vector $\mathbf{p}(t)$ can be written as a superposition of exponentially varying modes,

$$\mathbf{p}(t) = \sum_\alpha \mathrm{e}^{-t\lambda_\alpha} c_\alpha \mathbf{u}_\alpha, \tag{1}$$

where the initial state is represented as a linear combination of the eigenvectors $\mathbf{p}(0) = \sum_\alpha c_\alpha \mathbf{u}_\alpha$, and the coefficient c_α reflects how much a state aligns with $\mathbf{u}_\alpha$. Since $\mathbf{L}$ is positive semidefinite, the eigenvalues are non-negative, and the modes are either stationary or exponentially decaying with time. As each eigenvector represents a mode for the evolution of the state, modes associated with smaller eigenvalues λ_α decay more slowly and correspond to smoother eigenvectors.

This allows us to zoom out and look at the behavior of the system over longer timescales by defining a coarse-graining procedure of the graph Laplacian using timescale separation [3–5]. In essence, if the k-smallest eigenvalues are well separated from the remaining eigenvalues, such that we have a large gap $\delta_k = |\lambda_{k+1} - \lambda_k|$ in the spectrum, we can simplify the description of the system. This is because the eigenmodes associated with eigenvalues larger than λ_k become negligible for time-scales $t > 1/\lambda_{k+1}$, and we can describe the system by the k-slowest eigenmodes. They form a dominant subspace of the dynamics, which allows us to define a low-dimensional approximate description of the graph dynamics [4]. Thus, we only consider the contributions of the k-slowest modes, resulting in the coarse-grained Laplacian

$$\mathbf{L}_{(1)} = \sum_{\alpha:\lambda_\alpha \leqslant \lambda_k} \lambda_\alpha \mathbf{u}_\alpha \mathbf{u}_\alpha^\top, \tag{2}$$

which is represented in $\mathcal{S}_{(1)} = \mathrm{span}(\{u_\beta\}_{\beta:\lambda_\beta \leqslant \lambda_k})$. The entries of $\mathbf{L}_{(1)}$ indicate how similar two vertices in G are in the context of the remaining modes or from a zoomed-out perspective. This is because $(\mathbf{u}_\alpha \mathbf{u}_\alpha^\top)_{ij} = u_{\alpha i} u_{\alpha j}$ is the product of the eigenvector components associated with vertices i and j, which is the cosine similarity measure between these vertices within the mode u_α. Thus, the sign and magnitude of the components $u_{\alpha i}$ and $u_{\alpha j}$ directly translate through $u_{\alpha i} u_{\alpha j}$ to how similar vertices i and j are within the structural pattern captured by $\mathbf{u}_\alpha$. Consequently, $(\mathbf{L}_{(1)})_{ij} = \sum_{\alpha:\lambda_\alpha \leqslant \lambda_k} \lambda_\alpha u_{\alpha i} u_{\alpha j}$ is a "weighted average" of similarities between vertices i and j, with eigenvalues λ_α acting as the "weights."

The approximation error of the dynamics satisfies

$$\begin{aligned} \epsilon(t) &= \left\| \sum_\alpha \mathrm{e}^{-t\lambda_\alpha} \mathbf{u}_\alpha^\top \mathbf{p}(0) \mathbf{u}_\alpha - \sum_{\alpha:\lambda_\alpha \leqslant \lambda_k} \mathrm{e}^{-t\lambda_\alpha} \mathbf{u}_\alpha^\top \mathbf{p}(0) \mathbf{u}_\alpha \right\| \\ &\leqslant \mathrm{e}^{-t\lambda_{k+1}} \epsilon(0), \end{aligned} \tag{3}$$

where $\epsilon(0)$ is the initial error due to neglecting the fast modes. This error will decay exponentially with a rate of at least λ_{k+1}. Thus, the larger λ_{k+1}, the faster the decay of the $(k+1)$

modes, and the better the first k modes describe the system dynamics. Furthermore, a large gap δ_k leads to a faster decay of the fast modes relative to the slow ones, resulting in a clearer separation of timescales. Conversely, a small δ_k causes both fast and slow modes to contribute to the system dynamics for approximately the same duration, reducing the quality of the approximation. Thus, the quality of the approximation depends on both the decay rate λ_{k+1} of the neglected modes and the gap [3–5]. Adiabatic error control, as in the k-space RG, is not possible for finite heterogeneous graphs due to their discrete spectrum (scales). However, for graphs whose spectrum (scales) can be approximated as continuous in the large graph limit (see, e.g., Ref. [23]), a β function akin to Refs. [24,25] can be defined through a continuous formulation of Eq. (2) with the spectral density, and errors can be controlled. Thus, our method can be applied to systems with both discrete and continuous scales λ_k.

Using Eq. (2) and the definition of the graph Laplacian, we define

$$\mathbf{A}_{(1)} = \mathrm{diag}(\mathbf{L}_{(1)}) - \mathbf{L}_{(1)}, \tag{4}$$

where $\mathrm{diag}(\mathbf{L}_{(1)})$ is a diagonal matrix containing the diagonal of $\mathbf{L}_{(1)}$. A positive entry in $\mathbf{L}_{(1)}$ or a negative entry in $\mathbf{A}_{(1)}$ indicates that vertices are similar in G at a zoomed-out perspective and can be contracted. To illustrate this, we consider graph (I), which has a candidate gap δ_2 in the spectrum and consists of three 4-cliques with weights of 0.9, connected by edges with weights of 0.1 [see Figs. 2(a) and 2(b)]. The edges of $G_{(1)}$ that have negative weights are shown in blue in Fig. 2(b). To perform the contraction, we assign the respective similarity values from $\mathbf{A}_{(1)}$ as weights to $\mathbf{A}$, resulting in $\mathbf{A}_{(2)}$ with

$$(\mathbf{A}_{(2)})_{ij} = \begin{cases} (\mathbf{A}_{(1)})_{ij} & \text{if } (\mathbf{A})_{ij} > 0, \\ 0 & \text{otherwise.} \end{cases} \tag{5}$$

Thereby, we only consider the weights of $\mathbf{A}_{(1)}$ from connections that also existed in $\mathbf{A}$. Then, we consider the corresponding "graph" $G_{(2)} = (V_{(2)}, E_{(2)})$ [see Fig. 2(b)]. We contract the vertices $i \in V_{(2)}$ and $j \in V_{(2)}$ connected by a negative edge weight into effective vertices s, where s remains connected to the vertices to which i and j were connected to. This results in the graph $G_{(3)} = (V_{(3)}, E_{(3)})$, which has the vertex set $V_{(3)} = (V_{(2)} \setminus \{i, j\}) \bigcup s$ and $E_{(3)} = (E_{(2)} \setminus \{\text{edges incident to } i \text{ or } j\}) \bigcup \{(x, s_m \in s) : (x, i) \in E_{(2)} \vee (x, j) \in E_{(2)}\}$, which preserves the structure of G at a zoomed-out perspective [see Fig. 2(b)]. For $\lambda_k \to 0$, Eq. (2) indicates that we will remain with the eigenvector associated with the eigenvalue zero, which tells us that all vertices are similar, and thus end up with a graph with one effective vertex. Conversely, for $\lambda_k \to \infty$, Eq. (2) indicates that no eigenvectors are removed, and we remain with the original graph.

Intuitively, coarse graining zooms out and decreases the resolution. Thus, we rescale the coarse-grained adjacency matrix $\mathbf{A}_{(3)}$ associated with $G_{(3)}$,

$$\mathbf{A}_R = \frac{1}{\lambda_k}\mathbf{A}_{(3)}, \tag{6}$$

which restores the original resolution. This means that the dynamics of the original system are approximately preserved in the renormalized system G_R. Since dynamical processes provide a notion of distance, this is analogous to the RG, where coarseg raining decreases the system size and increases the lattice spacing, while rescaling restores the original dimensions. From another perspective, rescaling ensures that the relative size of fluctuations in this system matches those of the original system. In contrast to RG schemes used in translationally invariant spaces, which are independent of the model they renormalize, our procedure deals with different heterogeneous spaces that lack such invariance. Consequently, when removing modes that reflect the graph's structure, dynamics must be incorporated. The modes of $\mathbf{L}$ encode both the dynamics and topology, rendering the procedure not purely topological and, thus, model dependent.

We compare the dynamics of the original graph and the corresponding renormalized graph in Figs. 2(c) and 3(c). In the original graph G, vertices contracted into effective vertices are highlighted by the colored circles. With Eq. (1), the states $\mathbf{p}(t)$ are determined, where $\mathbf{p}(0)$ is a vector with all entries set to zero except for a value of 1 at one of the vertices within the red-highlighted cluster. This is repeated for all vertices within the red cluster, and the average is computed. These values are compared with the states of the renormalized graph G_R, where $\mathbf{p}(0)$ is a vector with all entries set to zero except for a value of 1 corresponding to the effective vertex highlighted in red. We compare to the graph G_{LRG} obtained from Ref. [2]'s Wilsonian LRG formulation, with the cutoff determined by the peak of the specific heat [2,10]. Our method and the Wilsonian LRG preserve the underlying dynamics well in this example. However, the differences become significant for more complex graphs, as we will see for graph (II). If multiple characteristic scales λ_k are present in the system, then by obtaining a renormalized graph for each, we gradually move from the microscopic to the macroscopic. This is shown in Fig. 3(b) for a Barabási-Albert graph (II) with 24 vertices, where the thick edges have weights of

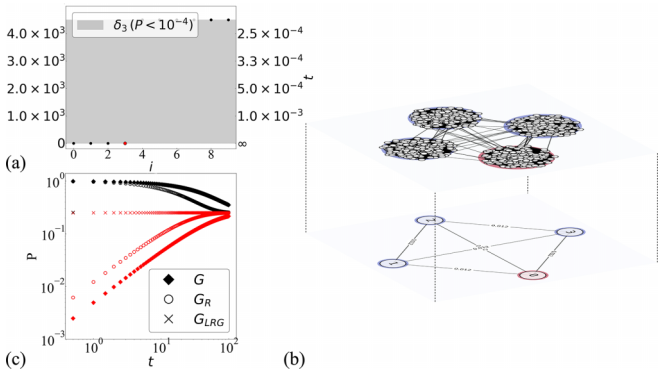


FIG. 4. Gap, dynamics, and renormalization of graph (III). (a), (b) A renormalized graph is obtained for the first candidate (p-value < 0.01) gap. (c) The states $\mathbf{p}(t)$ of the clusters (original graph G) and effective vertices (renormalized graphs G_R or G_{LRG}) are determined by Eq. (1), with $\mathbf{p}(0)$ representing the cluster or effective vertex highlighted in red. The graph G_R is obtained using our renormalization procedure with $\lambda_3 = 0.02$, while G_{LRG} is obtained using Ref. [2]'s Wilsonian LRG with $\lambda^* = 1/0.1$ (identified by specific-heat peak [2]). Closer alignment between points of the same color of G_R or G_{LRG} with G indicates better preservation of dynamics.

0.9, and the thin edges have weights of 0.1. Each renormalized graph in Fig. 3(b) preserves the zoomed-out structure of the graph, i.e., the skeleton. For the first candidate gap $\lambda_6 = 0.12$, seven effective vertices representing clusters in the original graph G are formed. These effective vertices provide insight into each scale's characteristic structures. In comparison, the Louvain community detection algorithm finds similar communities, except it detects {2, 6, 9, 10, 12, 22} as one community. This is because it uses modularity optimization, which has a resolution limit [26]. Additionally, not only the zoomed-out structure but also the dynamics of the original graph are approximately preserved [see Fig. 3(c)]. A detailed comparison in Appendix D underscores that renormalization captures not merely communities but rather characteristic structures across scales to generate an effective representation. For a detailed comparison of structure and dynamics preservation with respect to Ref. [2], including validation that dynamics preservation is not attributable to randomness; see Appendices B and C. For systems with large-scale structures, anomalous gaps typically appear among the smallest eigenvalues of the spectrum [3,4]. Our method therefore computes eigenpairs iteratively—starting with the smallest—until a candidate gap is detected and thereby avoids computing the entire spectrum. This makes our renormalization procedure well suited for such large systems, as we demonstrate using a stochastic block model (III) with 2×10^4 vertices and 4.9×10^7 edges [see Fig. 4(b)]. Because the large-scale structure of graph (III) is fully connected, both our method and the LRG yield renormalized graphs—G_R and G_{LRG}—with identical structure but with different edge weights, where our method better preserves large-scale dynamics [as shown in Fig. 4(c)].

Furthermore, in Appendix A we demonstrate—using infrastructure, social, and mobility graphs—that the effective vertices of the renormalized graph associated with the candidate gap are meaningful and have intuitive interpretations, such as representing cities linked by major roads or neighboring airports.

Notably, in Ref. [27], a different perspective is taken on obtaining complexity-reduced representations that preserve Laplacian dynamics with error bounds by removing edges rather than removing both vertices and edges.

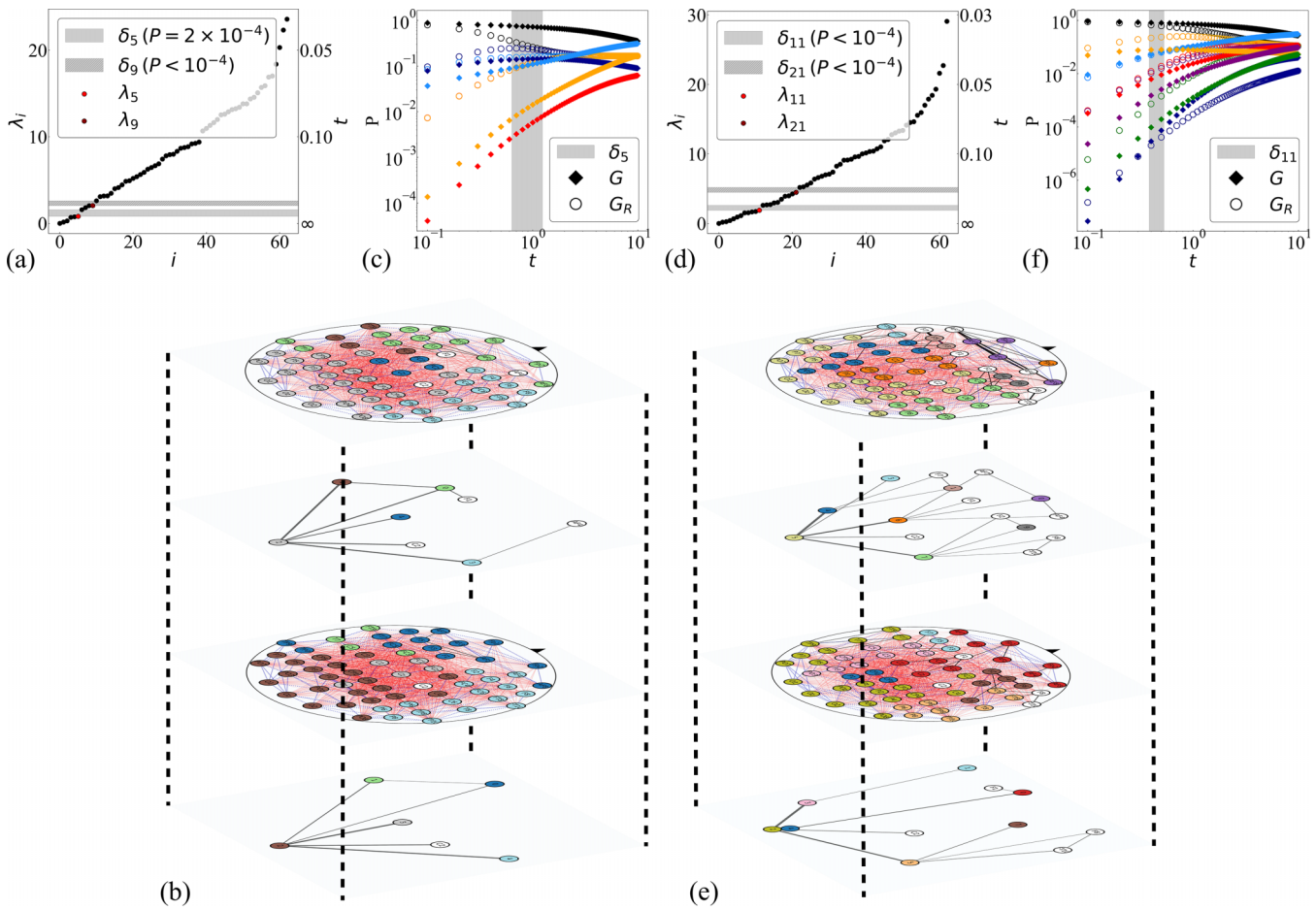


FIG. 5. Gap, dynamics, and renormalization of the brain. (a), (d) For each λ_k, corresponding to the first two candidate gaps (p value $<$ 0.01), a renormalized graph is obtained. (b), (e) The electrode map shows the clusters of electrodes that are contracted into effective vertices, with colors showing which cluster belongs to which effective vertex. The effective vertices representing the occipital lobe are the most central in the renormalized graphs. (c), (f) Dynamics in G_R corresponding to the first candidate gap and G are compared using Eq. (1). The initial state is the effective vertex or cluster representing the frontal lobe. Each color indicates a different effective vertex or cluster.

IV. HUMAN NEURAL NETWORK RENORMALIZATION

It is hypothesized that the brain self-organizes toward a critical state characterized by a high degree of scale invariance, exhibiting emergent properties and collective behaviors in neural activity across scales, such as neural avalanches [28–32]. To investigate this, we analyzed brain activity across scales by renormalizing triangulated maximally filtered graphs [33] extracted from the mutual information between electrode signals in Refs. [34,35]'s EEG recordings. Each vertex represented the activity of a neuron group, and edge weights were the mutual information between the vertices they connect. The recordings were from a study where participants identified images. They were divided into seven partitions: rest 1 and rest 2 (before and after the task) and attention 1–5 (during the task). As expected, the spectrum revealed multiple candidate gaps, indicating multiple characteristic scales [36] [see Figs. 5(a) and 5(d)]. This is typical for real-world systems represented by heterogeneous graphs (see Appendix A for examples). We obtained a renormalized graph for the λ_k corresponding to the first two candidate gaps. This is visualized in Figs. 5(b) and 5(e) for rest 1 and attention 1, which are representative of the brain's rest and attention states. In the renormalized graphs, we observe the formation of effective vertices that absorb clusters of vertices where information spreads fast, indicating groups of strongly interacting neurons. These clusters highlight regions with high mutual information, suggesting functional neuronal connectivity and coordinated neuronal activity. Contracting these clusters into effective vertices reduced the redundant information shared by the vertices, resulting in a simplified representation of brain activity with significantly fewer vertices. Both resting states exhibit the same number of effective vertices absorbing a few large clusters, while the attention states have more, suggesting less redundant activation patterns, more flexible and efficient information processing, and specialization in brain dynamics [37]. This is supported by the cluster shape. At rest, the cluster covering most electrodes corresponding to the occipital lobe {O1, O2, Oz, PO3, PO4, PO7, PO8}, spans a wide, circular area in the posterior part of the electrode map, including parts of the parietal lobe, indicating less specialized and more generalized brain activity. In contrast, the corresponding cluster during attention, while still covering the occipital region, is more compact and irregular in shape, concentrated with fewer electrodes. It represents a more specific functional grouping and indicates a more focused and specialized processing of information. We observe that the dynamics are better preserved for attention states compared to rest states [see Figs. 5(c) and 5(f)]. This is explained by λ_{k+1} being smaller for the rest states than for the attention states [see Eq. (3)]. This suggests that in rest states, macroscopic neural activation patterns do not align well with microscopic patterns, whereas for attention states, slow modes describe the pattern well across scales, indicating a higher degree of scale invariance.

V. CONCLUSIONS

We have introduced a graph renormalization procedure based on the coarse-grained Laplacian. For different scales, it generates representations with reduced complexity (fewer vertices), reducing redundant information while preserving both the dynamics and the zoomed-out topological structure. Since most graph algorithms run in polynomial time relative to the number of vertices, this method facilitates the analysis of large graphs. It has allowed us to study the macroscopic properties of brain activity emerging from the interactions of the system's microscopic constituents. We have observed collective behavior in the form of clusters of coordinated neuronal activity. Additionally, the renormalized graphs show that brain activity dynamically reorganizes across scales during the object recognition task, with more generalized activity during rest and more specialized activity in the occipital lobe during attention. Moreover, our results suggest that during attention the degree of scale invariance is higher, indicating that a simpler, more universal representation of neural dynamics can be found via renormalization.

ACKNOWLEDGMENTS

We thank Renaud Lambiotte for his significant contributions and insightful comments on the manuscript, and Andrea Gabrielli, Sabrina Aufiero, Peter Zhang, and Hongyu Lin for their helpful discussions. M.S. further acknowledges the financial support of the fellowship provided by University College London and PGIM.

DATA AVAILABILITY

Some of the data that support the findings of this article are openly available [34,35,38–42]. Data to support Figs. 1–4 and 9–18 are not publicly available. The data are available from the authors upon reasonable request.

APPENDIX A: GAPS AND COMMUNITIES IN REAL-WORLD GRAPHS

In addition to the graphs representing neuronal activity in the main text, we consider three additional real-world graph representations with heterogeneous topology. We demonstrate that they exhibit candidate gaps in the spectrum corresponding to meaningful structures, which are summarized by the effective vertices in the renormalized graph.

1. Facebook graph

The Facebook graph [38,41] consists of ten ego users and their friends. A user is represented as a vertex and can be connected to multiple ego vertices. The graph is connected, unweighted, and undirected with 4039 vertices and 88 234 edges. We renormalize it for λ_{104}, corresponding to the first candidate gap δ_{104} [see Fig. 6(a)]. The gap-specific threshold is $\alpha = 0.01$ and the gap-specific p value is computed with respect to 10^4 Erdős-Rényi graphs. We examine the vertices summarized by a randomly selected effective vertex and see they form meaningful clusters [see Fig. 6(b)]. Most belong exclusively to ego user 0, except that two vertices belong to ego users 0, 2, and 3.

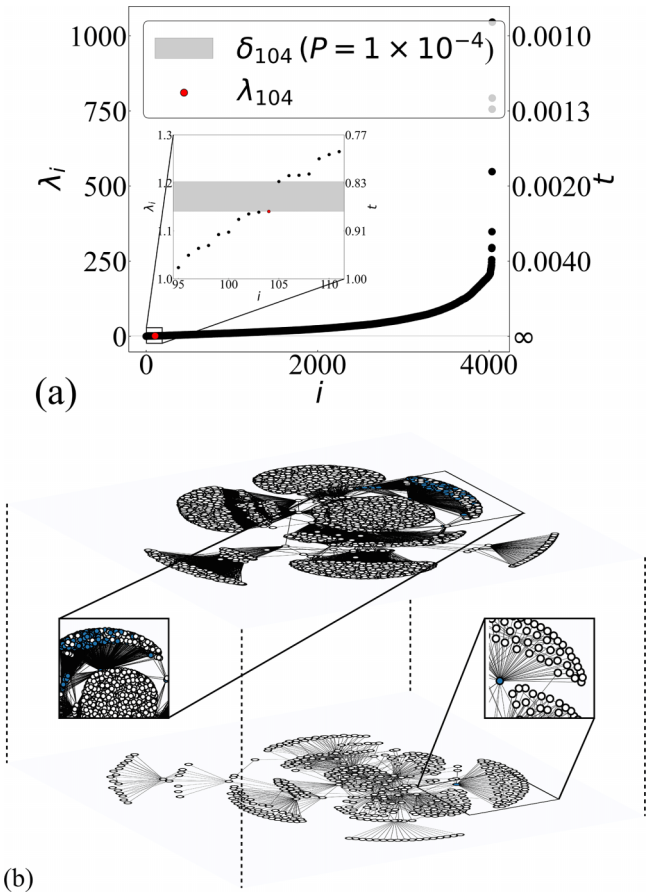


FIG. 6. Gap and vertices summarized by effective vertices in the renormalized Facebook graph. A renormalized graph is obtained for λ_{104}, corresponding to the first candidate (p-value < 0.01) gap δ_{104}. The randomly selected effective vertex contains users who exclusively belong to ego user 0, except for two that belong to ego users 0, 2, and 3 (dark blue).

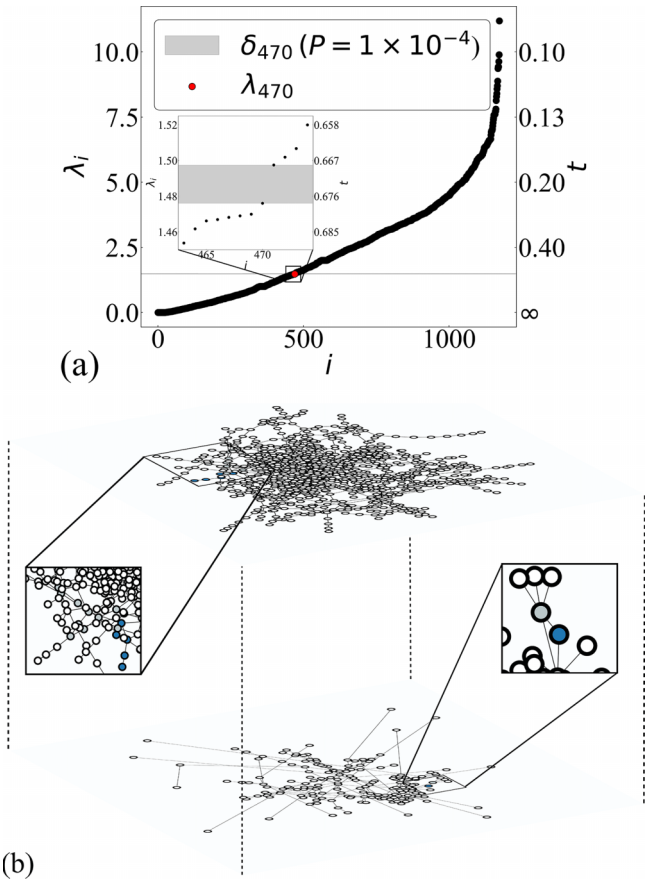


FIG. 7. Gap and vertices summarized by effective vertices in the renormalized Euroroad graph. A renormalized graph is obtained for λ_{470}, corresponding to the first candidate (p-value < 0.01) gap δ_{470}. The light-blue effective vertex contains the Italian cities Perugia, Fiano Romano, Rimini, Fano, Naples, Cesena, Canosa di Puglia, Ancona, Pescara, and Bari. The dark-blue effective vertex contains mostly Italian cities—Migliarino, Rome, Grosseto, Olbia—and one in Norway, Karesuvanto.

2. Euroroad graph

The second real-world graph is the Euroroad graph [39,42]. The vertices represent cities, and an edge connecting two vertices indicates that they are connected by a Euroroad. The graph is unweighted, undirected, and has 1174 vertices and 1417 edges. Isolated cities are removed, resulting in a connected graph of 1039 vertices and 1305 edges. We renormalize it for λ_{470}, corresponding to the first candidate gap δ_{470} [see Fig. 7(a)]. The gap-specific threshold is $\alpha = 0.01$, and the gap-specific p value is computed with respect to 10^4 Erdős-Rényi graphs. In Fig. 7(b), the light-blue vertices in the original graph correspond exclusively to cities within Italy, particularly in central and southern Italy. They are all summarized by an effective vertex in the renormalized graph, also highlighted in light blue. The dark-blue effective vertex in the renormalized graph represents mostly Italian cities, especially in central Italy and the island of Sardinia. Interestingly, one vertex belongs to a city in Finland, Karesuvanto. This is likely because it lies on a key route connecting Northern Europe and Southern Europe—namely, the European route E45 connecting Norway and Italy. In the renormalized graph, these two vertices are directly connected because the E45 also connects Naples and Karesuvanto. Thus, the renormalized graph represents the large-scale perspective of the Euroroad graph.

3. Air-route graph

The air-route graph [40] contains 67 663 routes between 3425 airports operated by 568 airlines spanning the globe. Vertices represent airports and edges represent flights connecting them. We treat the graph as undirected and discard the 28 isolated airports. The number of equal flights—where multiple airlines serve the same route—is included as the edge weight. We renormalize the graph for λ_{93}, corresponding to the first candidate gap δ_{93} [see Fig. 8(a)]. The gap-specific threshold is $\alpha = 0.01$, and the gap-specific p value is computed with respect to 10^4 Erdős-Rényi graphs. In Fig. 8(b), the dark-blue vertices represent airports in the Democratic Republic of the Congo, primarily in the eastern region.

Overall, real-world graphs with heterogeneous topology exhibit gaps due to meaningful structures.

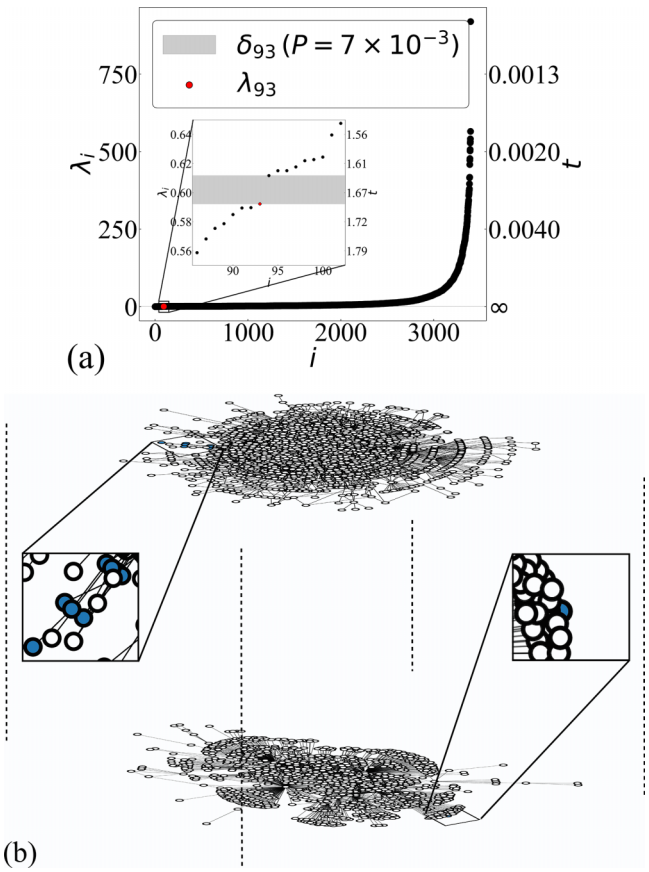


FIG. 8. Gap and vertices summarized by effective vertices in the renormalized air-route graph. A renormalized graph is generated for λ_{93}, corresponding to the first candidate (p-value < 0.01) gap δ_{93}. The dark-blue effective vertex includes airports in the Democratic Republic of the Congo: Bangoka International Airport, Bunia Airport, Kongolo Airport, Kalemie Airport, Kavumu Airport, Beni Airport, Matari Airport, and Goma International Airport.

APPENDIX B: PRESERVING DYNAMICS

We demonstrate that the preservation of dynamics by our renormalization procedure is not a consequence of randomness. We show this by using a null model that selects, uniformly at random, an edge connecting two vertices in the original graph G and then contracts those vertices. This process is repeated until the number of vertices equals that of the renormalized graph G_R. For the resulting randomly contracted graph G_0 and the renormalized graph G_R, we compute the dynamics as follows: given an initial state $\mathbf{p}(0)$, the state $\mathbf{p}(t)$ is computed for a range of dimensionless time steps t using Eq. (1) of the main text. This process is repeated for 10^4 instances of G_0, and for each t, the 10^4 resulting states $\mathbf{p}(t)$ are averaged elementwise and presented in Fig. 9.

We statistically validate whether the preserved dynamics of the renormalized graph G_R differ significantly from those of the randomly contracted graphs G_0 by computing an empirical p value. For G_R, we determine, for each effective vertex i, the area

$$A_i = \int p_i(t)\,\mathrm{d}t \approx \sum_k \frac{p_i(t_k) + p_i(t_{k+1})}{2}\,\Delta t, \qquad \text{(B1)}$$

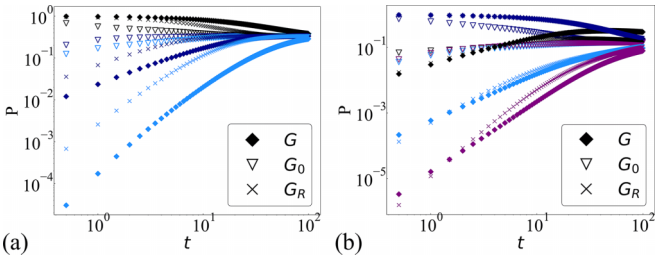


FIG. 9. Dynamics. The null model G_0 is generated by randomly contracting vertices connected by edges in the original graph G until it has the same number of vertices as the renormalized graph G_R. Ten thousand instances are generated and their dynamics—calculated using Eq. (1) of the main text—are compared to those of G_R to compute a p value. Each color represents a different effective vertex or cluster. (a) The dynamics of the graph (I) from the main text G, G_R, and G_0—specifically, the elementwise average of the 10^4 states $\mathbf{p}(t)$—starting from the cluster or effective vertex 0. (b) The dynamics of the graph (II) from the main text G, G_R, and G_0—specifically, the elementwise average of the 10^4 states $\mathbf{p}(t)$—starting from the cluster or effective vertex 1. For clarity, we omit the clusters and the corresponding effective vertices 3, 4, and 6. Closer alignment between points of the same color of G_R or G_0 with G indicates a better preservation of dynamics.

TABLE I. p values for graphs (I) and (II) are computed using an ensemble of 10^4 randomly contracted graphs with a significance threshold $\alpha = 0.05$. The initial state $\mathbf{p}(0)$ for graph (I) is defined as $p_0(0) = 1$ with all other entries set to zero, while for graph (II) it is defined as $p_1(0) = 1$ with all other entries set to zero.

ith element in $\mathbf{p}(t)$	p-value graph (I)	p-value graph (II)
$p_0(t)$	$<10^4$	2×10^{-3}
$p_1(t)$	4×10^{-1}	$<10^4$
$p_2(t)$	$<10^4$	1.1×10^{-2}
$p_5(t)$		1.0×10^{-3}

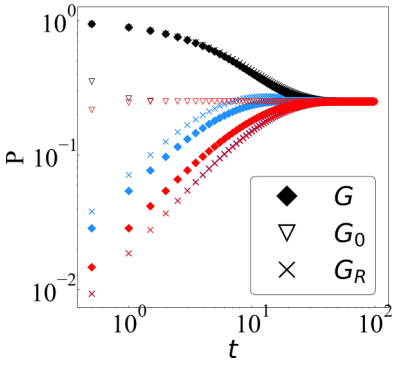


FIG. 10. Dynamics. The graph G_0 is generated by contracting known clusters in a stochastic block model. Each color represents a different effective vertex or cluster. The dynamics—calculated using Eq. (1) of the main text—of G, G_R, and G_0, starting from the cluster or effective vertex 0, are compared. Closer alignment between points of the same color of G_R or G_0 with those of G indicates that the dynamics are better preserved.

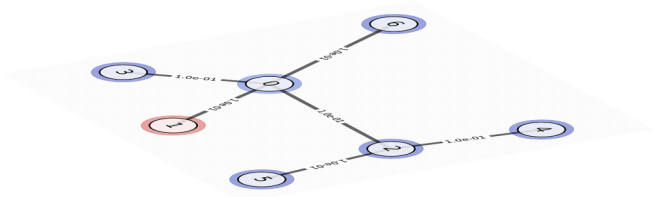


FIG. 11. Real-space LRG. For graph (II), a Barabási-Albert graph with $m = 1$ and 24 vertices, a renormalized graph is generated using the real-space LRG.

under the curve $p_i(t)$. In practice, we have a discrete time grid $\{t_k\}_k$ and therefore use the trapezoidal rule. We then compute the p value for each curve $p_i(t)$ by comparing its area with the areas obtained from 10^4 null-model instances:

$$A_i^{(j)} \approx \sum_k \frac{p_i^{(j)}(t_k) + p_i^{(j)}(t_{k+1})}{2} \Delta t. \qquad j = 1, \ldots, 10^4. \tag{B2}$$

Specifically, with the 10^4 areas $\{A_i^{(j)}\}_{j=1}^{10^4}$, we define the empirical cumulative distribution function:

$$F_i(a) = \frac{1}{10^4} \sum_{j=1}^{10^4} \mathbf{1}\{A_i^{(j)} \leqslant a\}, \tag{B3}$$

where $\mathbf{1}\{\cdot\}$ denotes the indicator function, and use the two-sided p value,

$$p \text{ value}_i = 2 \min\left[F_i(A_i), 1 - F_i(A_i)\right]. \tag{B4}$$

We set the significance threshold to $\alpha = 0.05$, and if the p value is less than α, we conclude that the preservation of dynamics by our renormalization procedure is significantly different from random.

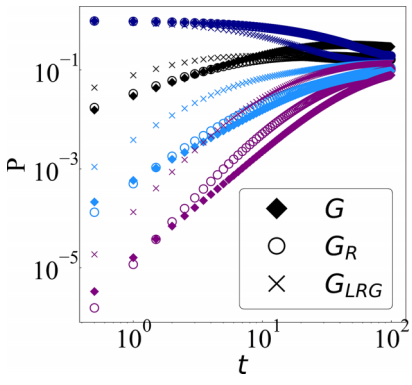


FIG. 12. Dynamics. The dynamics of the graph (II), renormalized using the real-space LRG (G_{LRG}) for $\tau^* = 2.79$ and our method (G_R) for λ_6, are compared to those of the original graph G. The states $\mathbf{p}(t)$ of the clusters in G and effective vertices in G_R or G_{LRG} are determined by Eq. (1) of the main text, with $\mathbf{p}(0)$ representing the cluster or effective vertex highlighted in red. Each color represents a different effective vertex or cluster. For clarity, clusters and the corresponding effective vertices 3, 4, and 6 are omitted. Closer alignment between points of the same color of G_R or G_{LRG} with G indicates that the dynamics are better preserved.

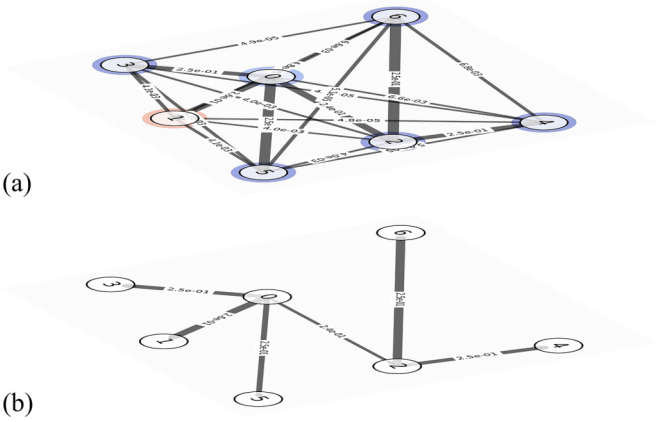


FIG. 13. k-space LRG and thresholding. For graph (II), a Barabási-Albert graph with $m = 1$ and 24 vertices, a renormalized graph is generated using the k-space LRG with $\tau^* = 2.79$ [2]. The first graph is generated without thresholding and the second graph is generated with thresholding.

Synthetic graphs

For graphs (I) and (II) of the main text, we observe that the preservation of the dynamics by our renormalization procedure is not due to randomness (see Fig. 9), as further confirmed by the p values (see Table I). The p values are all smaller than the significance threshold α, except for graph (I) for the entry $p_1(t)$. The reason for not having a p value below the threshold is likely due to the graph's simple structure. Next, we compare to a cluster coarse-graining procedure that contracts known communities in an unweighted stochastic block model. The graph consists of 256 vertices divided into 4 equal modules, each with an intramodule connectivity probability $p = 0.78$ and an intermodule connectivity probability $q = 5 \times 10^{-4}$. This procedure generates a fully connected graph with 4 vertices, where each edge has a weight of 1—analogous to the graph generated using the real-space LRG [see Fig. 14(a)]. We renormalize the stochastic block model for λ_3, corresponding to the candidate gap δ_3 [see Fig. 14(a)], and obtain G_R. From the comparison in Fig. 10, we conclude that our method preserves the large-scale dynamics of the graph more accurately than a cluster coarse-graining procedure.

APPENDIX C: COMPARISON TO THE LRG

In Ref. [2], two approaches are proposed—the real-space and the k-space formulations—both of which rely on a normalized heat kernel to identify clusters of vertices strongly linked by diffusion at a timescale identified by the specific heat (the derivative of the normalized heat kernel's entropy).

The real-space formulation generates a coarser representation of a graph's structure based on the clusters determined by the normalized heat kernel and a ratio. However, the edge weights between the supernodes representing these clusters are not adjusted with respect to the timescale. Since interactions are scale dependent [7,9], the original graph's dynamics are not well preserved in the renormalized graph [see Figs. 14(b) and 12)].

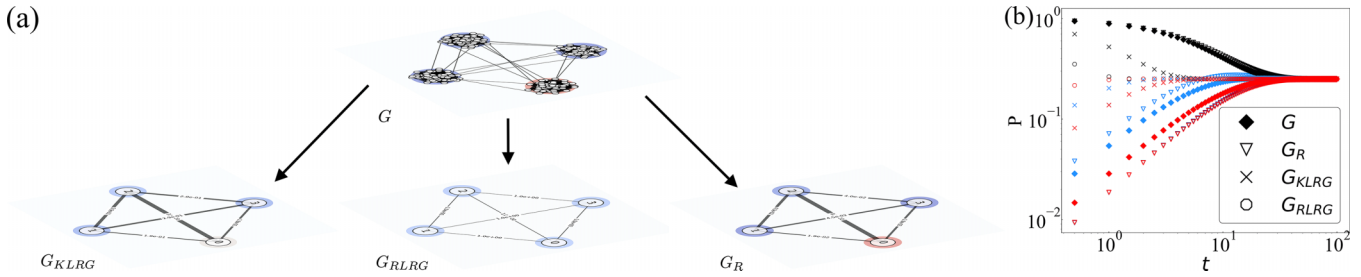


FIG. 14. Stochastic block model renormalization and dynamics. (a) Representations of the stochastic block model are generated, with the k-space LRG (G_{KLRG}), the real-space LRG (G_{RLRG}), and our renormalization procedure (G_R). (b) The states $\mathbf{p}(t)$ of the clusters in G and effective vertices in G_R or G_{LRG} are determined by Eq. (1) of the main text, with $\mathbf{p}(0)$ representing the cluster or effective vertex 0. Each color represents a different effective vertex or cluster. Closer alignment between points of the same color of G_R, or G_{RLRG}, or G_{KLRG} with G indicates that the dynamics are better preserved.

The k-space formulation also identifies clusters leveraging the normalized heat kernel. A projection of a coarse-grained Laplacian onto these clusters results in a graph that is fully connected and can have negative edge weights [see Fig. 13(a)]. The large-scale structure is not preserved, nor are the original graph's dynamics preserved as accurately as with our method [see Figs. 14(b) and 2(c) of the main text]. Moreover, thresholding—as proposed in Ref. [2]—is not straightforward, as the threshold must be determined for each case and does not guarantee the preservation of the large-scale structure [see Fig. 13(b)]. In contrast, our procedure generates an effective representation that preserves both large-scale structure and dynamics by examining how interactions (edge weights) between effective degrees of freedom (effective vertices) change with the scale λ_k and adjusting them. We identify the relevant scales λ_k, groups of vertices that can effectively be represented as a single vertex (effective vertex) at the scale λ_k, and the edge weights between them using the graph Laplacian itself.

2. Barabási-Albert graph

Graph (II) is a Barabási-Albert graph with the parameters from Ref. [2] ($m = 1$ and 24 vertices). A renormalized graph is generated as described in Ref. [2] using the specific heat C and the rule proposed over $\tau \sim \tau^*$, where τ^* denotes the C peak at short times. We obtain $\tau^* = 2.79$, resulting in the renormalized graph shown in Fig. 11. In Fig. 2(b) of the main text, the graph is renormalized using our procedure, and its structure is identical, with the same clusters of vertices represented by effective vertices. In the renormalized graph generated by the real-space LRG, the edge weights between the supernodes are not adjusted. Consequently, although the large-scale structure of the graph is preserved, the diffusion dynamics are not well preserved (see Fig. 12). For $\tau^* = 2.79$,

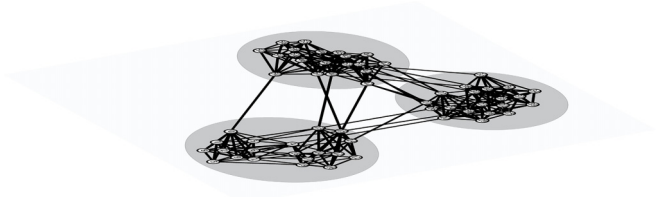


FIG. 15. Clusters in the hierarchical modularity graph are identified using the Louvain algorithm and highlighted in gray. The graph has 4 top-level modules of 20 vertices each. One module is subdivided into two sublevel modules, with the first consisting of vertices 0–10 and the second of vertices 11–20. Each of the three identified clusters corresponds to one of the top-level modules.

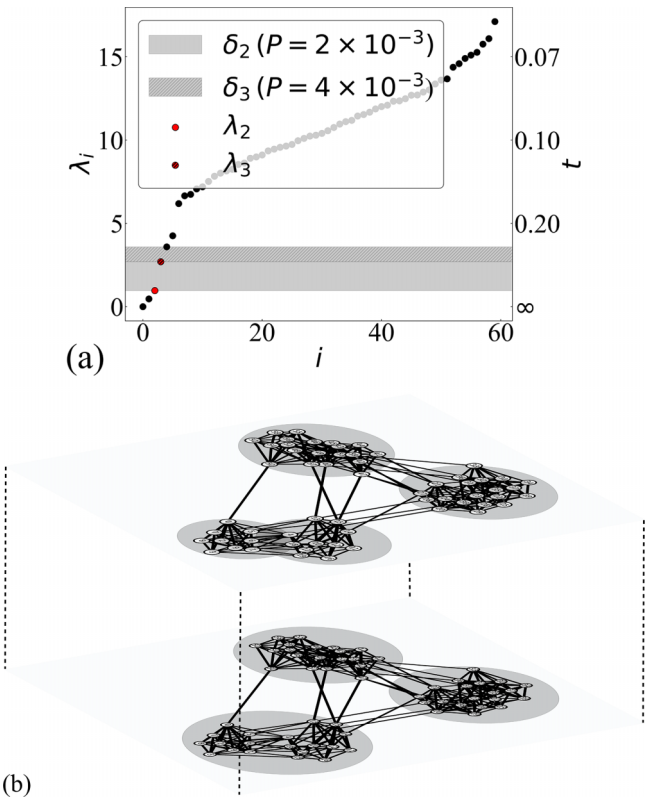


FIG. 16. Gaps in the spectrum of a hierarchical modularity graph, as well as vertices summarized by effective vertices in the renormalized graph, are highlighted in gray. The graph has 4 top-level modules of 20 vertices each, where one is subdivided into two sublevel modules: vertices 0–10 and 11–20. The first graph highlights the vertices summarized by the effective vertices of the renormalized graph for λ_2, which capture the two top-level and sublevel modules. The second graph highlights the vertices summarized by the effective vertices of the renormalized graph for λ_3, with each effective vertex absorbing one of the three top-level modules.

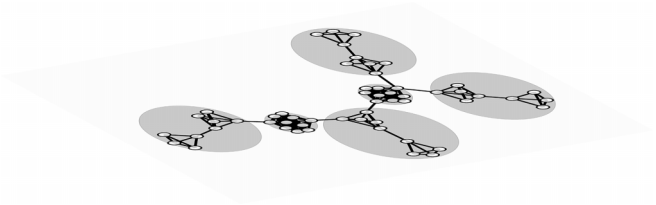


FIG. 17. Clusters in the heterogeneous clique-size graph are identified using the Louvain algorithm and highlighted in gray. Although the two 10-cliques are identified, the 5-cliques and 4-cliques are merged into one community.

we obtain a renormalized representation of graph (II) using the k-space LRG as described in Ref. [2], which is fully connected [see Fig. 13(a)]. We also apply thresholding. Since there is no obvious threshold, we set it with respect to the real-space LRG so that the six strongest edges are retained. In both cases, with and without thresholding, the resulting graph does not reflect the large-scale structure of the original graph [see Fig. 13(b)]. A comparison between our method and the k-space LRG in terms of preserving diffusion dynamics of graph (II) is presented in Fig. 2 of the main text, demonstrating that our method is more accurate.

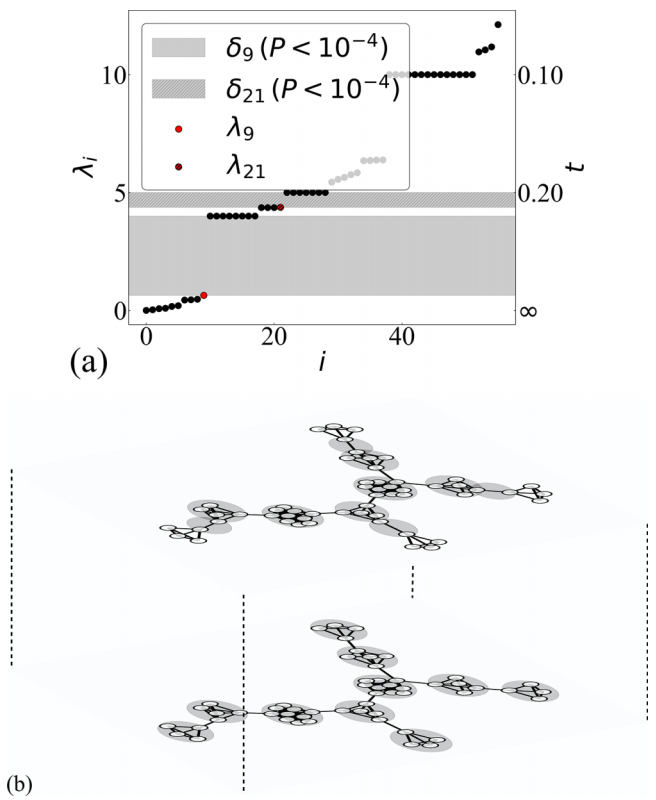


FIG. 18. Gaps in the spectrum of the heterogeneous clique-size graph, as well as vertices summarized by effective vertices in the renormalized graph, are highlighted in gray. The original graph consists of two 10-cliques, one connected to two 5-cliques and the other to three 5-cliques, and each 5-clique is connected to a single 4-clique. The first graph shows the vertices summarized by the effective vertices of the renormalized graph for λ_{21}. Two of these effective vertices each summarize one of the two 10-cliques. Each of the 5-cliques is summarized by an effective vertex, and the vertices connecting the 4-cliques to the 5-cliques are also summarized into an effective vertex. The effective vertices corresponding to the 5-cliques are merged with the effective vertices corresponding to the 4-cliques. The second graph highlights the vertices summarized by the effective vertices of the renormalized graph for λ_9, where each effective vertex summarizes one of the cliques.

3. Stochastic block model

We consider the stochastic block model from the supplemental material of [2] with 256 vertices divided into 4 equal modules, each with an intramodule connectivity probability $p = 0.78$ and an intermodule connectivity probability $q = 5 \times 10^{-4}$. We generated renormalized representations using the real-space and k-space LRG for $\tau^* = 0.1$, and our renormalization procedure for λ_3 corresponding to the candidate gap δ_3. Our procedure preserves the original large-scale dynamics more accurately than both the real-space and the k-space LRG. Because the large-scale structure is a fully connected graph, no thresholding is required for the k-space renormalized graph [see Fig. 14(a)]. The graph generated by the real-space LRG is the same one that would be obtained by contracting the clusters identified by clustering algorithms such as Louvain.

APPENDIX D: COMPARISON TO LOUVAIN

Renormalization differs from conventional clustering methods, such as Louvain. It captures characteristic structures across scales rather than merely clusters, to generate an effective graph representation. This is demonstrated by comparing the procedure with Louvain on two additional examples. Furthermore, the renormalization procedure can uncover clusters at different scales that the Louvain clustering algorithm cannot detect. In hierarchical (multiscale) graphs with multiple levels of organization, smaller communities or deeper hierarchies are merged and thus overlooked by Louvain if merging them does not significantly lower the modularity score. The resolution limit of modularity-based clustering has been extensively discussed in Refs. [26,43–45]. Renormalization, on the other hand, does not have this problem. The following examples and Fig. 2(b) in the main text demonstrate the ability to zoom out to each characteristic scale λ_k.

1. Hierarchical modularity graph

In the first example, a two-level hierarchical modularity graph with four modules is considered. The probability that vertices within the same module are connected is 0.95. Among these four modules, three are top-level modules of 20 vertices each, while the fourth is subdivided into two sublevel modules of 10 vertices each. The first sublevel module consists of vertices 0–10, and the second consists of vertices 11–20. The probability of an edge between sublevel modules is 0.2, and the probability of an edge between top-level modules is 0.01. The Louvain algorithm identifies the three top-level modules but not the two sublevel modules (see Fig. 15). The renormalization procedure generates two effective representations: The first for λ_3, corresponding to gap δ_3 [see Fig. 16(a)], and the second for λ_2, corresponding to gap δ_2 [see Fig. 16(a)]. The

first representation has four effective vertices, each summarizing one of the two top-level modules and the two sublevel modules [highlighted in gray in Fig. 16(b)]. The second representation has three effective vertices, each summarizing one of the top-level modules [highlighted in gray in Fig. 16(b)].

2. Heterogeneous clique-size graph

Next, we consider a graph consisting of two 10-cliques, with one connected to two 5-cliques and the other connected to three 5-cliques. Additionally, each 5-clique is connected to a single 4-clique. The Louvain algorithm identifies the two 10-cliques but fails to distinguish the 5-cliques from the 4-cliques, merging them into one community (see Fig. 17). The renormalization procedure generates two renormalized graphs: the first for λ_{21}, corresponding to gap δ_{21} [see Fig. 18(a)], and the second for λ_9, corresponding to gap δ_9 [see Fig. 18(a)]. The first renormalized graph has six effective vertices. Two of these effective vertices each summarize one of the two 10-cliques. Each of the four 5-cliques is summarized by an effective vertex, and the vertices connecting the 4-cliques to the 5-cliques are also summarized into an effective vertex. Because the effective vertices corresponding to the 5-cliques are essentially merged with the effective vertices corresponding to the 4-cliques, each clique is represented by an effective vertex in the renormalized graph, except for the four 4-cliques [see Fig. 18(b)]. The renormalization procedure, in addition to identifying clusters, also identifies the "connectors" between the clusters to generate the effective representation for the scale λ_{21}. The second renormalized graph has ten effective vertices, each summarizing one of the cliques [see Fig. 18(b)].

In conclusion, renormalization captures characteristic structures across scales in order to generate an effective representation.

[1] K. G. Wilson and J. Kogut, Phys. Rep.. **12**, 75 (1974).
[2] P. Villegas, T. Gili, G. Caldarelli, and A. Gabrielli, Nat. Phys. **19**, 445 (2023).
[3] F. R. K. Chung, *Spectral Graph Theory*, Conference Board of the Mathematical Sciences (American Mathematical Society, Providence, R.I. 1997).
[4] R. Lambiotte and M. T. Schaub, *Modularity and Dynamics on Complex Networks*, Elements in the Structure and Dynamics of Complex Networks (Cambridge University Press, Cambridge 2022).
[5] S. Strogatz, *Nonlinear Dynamics and Chaos: With Applications to Physics, Biology, Chemistry and Engineering*, Studies in Nonlinearity (Westview, Cambridge, MA, 2000).
[6] M. De Domenico and J. Biamonte, Phys. Rev. X **6**, 041062 (2016).
[7] L. P. Kadanoff, Phys. Phys. Fiz. **2**, 263 (1966).
[8] K. G. Wilson, Rev. Mod. Phys. **47**, 773 (1975).
[9] K. G. Wilson, Sci. Am. **241**, 158 (1979).
[10] P. Villegas, A. Gabrielli, F. Santucci, G. Caldarelli, and T. Gili, Phys. Rev. Res. **4**, 033196 (2022).
[11] G. Cimini, T. Squartini, F. Saracco, D. Garlaschelli, A. Gabrielli, and G. Caldarelli, Nat. Rev. Phys. **1**, 58 (2019).
[12] A. Poggialini, P. Villegas, M. A. Muñoz, and A. Gabrielli, Phys. Rev. Lett. **134**, 057401 (2025).
[13] A. Gabrielli, D. Garlaschelli, S. P. Patil, and M. A. Serrano, Nat. Rev. Phys. **7**, 203 (2025).
[14] N. Masuda, M. A. Porter, and R. Lambiotte, Phys. Rep. **716-717**, 1 (2017).
[15] J. Ambjørn, J. Jurkiewicz, and R. Loll, Phys. Rev. Lett. **95**, 171301 (2005).
[16] G. García-Pérez, M. Boguñá, and M. Á. Serrano, Nat. Phys. **14**, 583 (2018).
[17] G. Calcagni, D. Oriti, and J. Thürigen, Class. Quantum Grav. **31**, 135014 (2014).
[18] G. Stewart and J. Sun, *Matrix Perturbation Theory*, Computer Science and Scientific Computing (Academic Press, Boston, MA, 1990).
[19] U. von Luxburg, Stat. Comput. **17**, 395 (2007).
[20] A. Ng, M. Jordan, and Y. Weiss, in *Advances in Neural Information Processing Systems* (MIT Press, 2001), Vol. 14.
[21] R. Milo, S. Shen-Orr, S. Itzkovitz, N. Kashtan, D. Chklovskii, and U. Alon, Science **298**, 824 (2002).
[22] S. Wernicke, IEEE/ACM Trans. Comput. Biol. Bioinf. **3**, 347 (2006).
[23] R. Burioni and D. Cassi, Phys. Rev. Lett. **76**, 1091 (1996).
[24] K. G. Wilson, Rev. Mod. Phys. **55**, 583 (1983).
[25] M. Gell-Mann and F. E. Low, Phys. Rev. **95**, 1300 (1954).
[26] S. Fortunato and M. Barthélemy, Proc. Natl. Acad. Sci. USA **104**, 36 (2007).
[27] D. A. Spielman and S.-H. Teng, SIAM J. Comput. **40**, 981 (2011).
[28] T. Mora and W. Bialek, J. Stat. Phys. **144**, 268 (2011).
[29] P. Bak, C. Tang, and K. Wiesenfeld, Phys. Rev. Lett. **59**, 381 (1987).
[30] N. Friedman, S. Ito, B. A. W. Brinkman, M. Shimono, R. E. Lee DeVille, K. A. Dahmen, J. M. Beggs, and T. C. Butler, Phys. Rev. Lett. **108**, 208102 (2012).
[31] J. M. Beggs and D. Plenz, J. Neurosci. **23**, 11167 (2003).
[32] L. Kuśmierz, S. Ogawa, and T. Toyoizumi, Phys. Rev. Lett. **125**, 028101 (2020).
[33] G. P. Massara, T. Di Matteo, and T. Aste, J. Complex Networks **5**, 161 (2016).
[34] A. T. Gifford, K. Dwivedi, G. Roig, and R. M. Cichy, NeuroImage **264**, 119754 (2022).
[35] A. T. Gifford, A large and rich EEG dataset for modeling human visual object recognition (2021), doi:10.17605/OSF.IO/3JK45.
[36] E. T. Bullmore and O. Sporns, Nat. Rev. Neurosci. **10**, 186 (2009).
[37] W. L. Shew, H. Yang, S. Yu, R. Roy, and D. Plenz, J. Neurosci. **31**, 55 (2011).
[38] J. Leskovec and J. Mcauley, in *Advances in Neural Information Processing Systems*, edited by F. Pereira, C. Burges, L. Bottou, and K. Weinberger (Curran Associates, Inc., 2012), Vol. 25.
[39] J. Kunegis, in *Proceedings of the 22nd International Conference on World Wide Web*, WWW '13 Companion

(Association for Computing Machinery, New York, 2013), pp. 1343–1350.

[40] OpenFlights Airport, airline, and route data, https://openflights.org (2025), Accessed 2025-03-04. Licensed under the Open Database License (ODbL) v1.0.

[41] J. Mcauley and J. Leskovec, *Facebook graph dataset*, Stanford Large Network Dataset Collection (SNAP) (2012), https://snap.stanford.edu/data/egonets-Facebook.html.

[42] J. Kunegis, *Euroroad graph dataset*, Koblenz Network Collection (KONECT), (2013), http://konect.uni-koblenz.de/networks/subelj_euroroad.

[43] A. Lancichinetti and S. Fortunato, Phys. Rev. E **84**, 066122 (2011).

[44] V. D. Blondel, J.-L. Guillaume, R. Lambiotte, and E. Lefebvre, J. Stat. Mech.: Theory Exp. (2008) P10008.

[45] S. Fortunato, Phys. Rep. **486**, 75 (2010).